

A 0.46-THz 25-Element Scalable and Wideband Radiator Array With Optimized Lens Integration in 65-nm CMOS

Hossein Jalili^{ID}, Member, IEEE, and Omeed Momeni, Senior Member, IEEE

Abstract—In this article, we present a 438–479-GHz fully integrated 25-element radiator array source based on a scalable structure of coupled standing wave oscillator cells without extra loss and parasitics from coupling networks. The bandwidth is extended using a varactor-less frequency tuning method, and EIRP is improved by increasing the size of the array using the proposed scalable coupling method and maximizing the radiation directivity using a silicon lens in an optimized radiation setup. An analysis of the radiation directivity of a chip-lens setup is presented as well as the employed approach for enhancing EIRP by maximizing the directivity. The circuit is implemented in a 65-nm CMOS process and is measured to have 40.7 GHz/8.9% frequency tuning range. The chip consumes 0.38–2.34-W power (1.18 W at 459-GHz center frequency) from a 1.2-V supply voltage. The circuit provides a maximum of −1.8-dBm radiated power and 19.3-dBm EIRP at 448 GHz using a 12.5-mm radius silicon lens. The minimum measured phase noise at 10-MHz offset is −100.6 dBc/Hz. To the best of our knowledge, this article has the largest EIRP, radiated power, and bandwidth among fully integrated silicon-based coherent sources above 350 GHz.

Index Terms—Coherent source, harmonic voltage controlled oscillator (VCO), millimeter-wave (mm-wave)/terahertz (THz), on-chip antenna, radiator array, silicon lens, standing wave, THz radiation, varactor-less frequency tuning, wideband.

I. INTRODUCTION

THE millimeter-wave (mm-wave)/terahertz (THz) spectrum offers promising potentials [1], [2] in various applications such as spectroscopy [3]–[5], imaging [6]–[10], radar [11], [12], and high-speed communication [13]–[16]. Implementing such systems in reliable low-cost silicon technologies requires sources that are capable of producing sufficient power levels in a wide bandwidth. However, several challenges need to be overcome in this endeavor. As we move toward the mm-wave/THz band, the maximum oscillation frequency (f_{\max}) of the process limits the power that can be generated by transistors. At the same time, losses of passives in the circuit increase and poor quality factor of varactors restricts the frequency of operation and tuning range. Fig. 1 shows

Manuscript received November 3, 2019; revised January 18, 2020 and March 25, 2020; accepted April 20, 2020. Date of publication May 8, 2020; date of current version August 26, 2020. This article was approved by Associate Editor Kenichi Okada. This work was supported by the National Science Foundation under Award 1454732. (Corresponding author: Hossein Jalili.)

The authors are with the Department of Electrical and Computer Engineering, University of California at Davis, Davis, CA 95616 USA (e-mail: hjalili@ucdavis.edu; omomeni@ucdavis.edu).

Color versions of one or more of the figures in this article are available online at <http://ieeexplore.ieee.org>.

Digital Object Identifier 10.1109/JSSC.2020.2989897

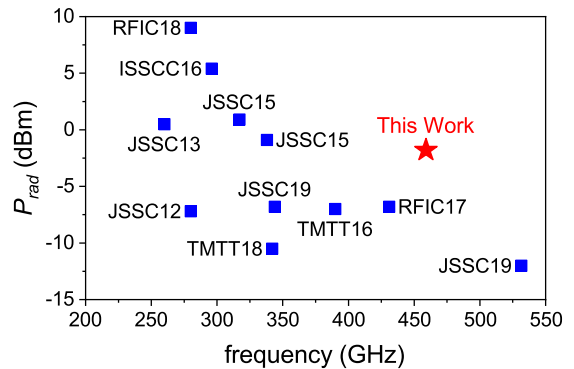


Fig. 1. Overview of the published radiated power levels among state-of-the-art integrated coherent sources in silicon.

an overview of the reported levels of radiated power (P_{rad}) among published state-of-the-art coherent sources in silicon technology and illustrates the increasing challenge of power generation and radiation as we approach the THz spectrum.

Frequency multipliers [17]–[19] and harmonic oscillators [20]–[32] are the main solutions for reaching frequencies above f_{\max} of the transistors. However, multipliers are generally more power hungry and less efficient. An array of coherent harmonic oscillators [5], [6], [20]–[27] is often employed in order to improve the output power level. Scalability and the level of extra loss and parasitics penalties are important factors in the choice of the array structure. Various techniques have been used in the published literature to synchronize the sources within an array. Extra quadrature oscillators are used in [5] to couple the main oscillators of the source. These coupling oscillators add to the parasitics and power consumption of the circuit but do not contribute to the radiated power. In [6], passive coupling is used for oscillators in each row of the array and individual rows are synchronized through phase locking to a reference signal by incorporating a phase-locked loop (PLL). Wireless subharmonic injection locking technique is employed in [20] which requires an additional fundamental frequency (100 GHz) external radiation source. In [26], a reference signal is symmetrically routed and used for injection locking of the sources in the array after going through phase-shifting and multiplication stages. We previously demonstrated in [25] the potential advantages of employing a standing wave oscillator (SWO) for scalable and wideband THz power generation.

As the frequency approaches the THz spectrum, the diminishing size of the antennas as well as the increasing loss of

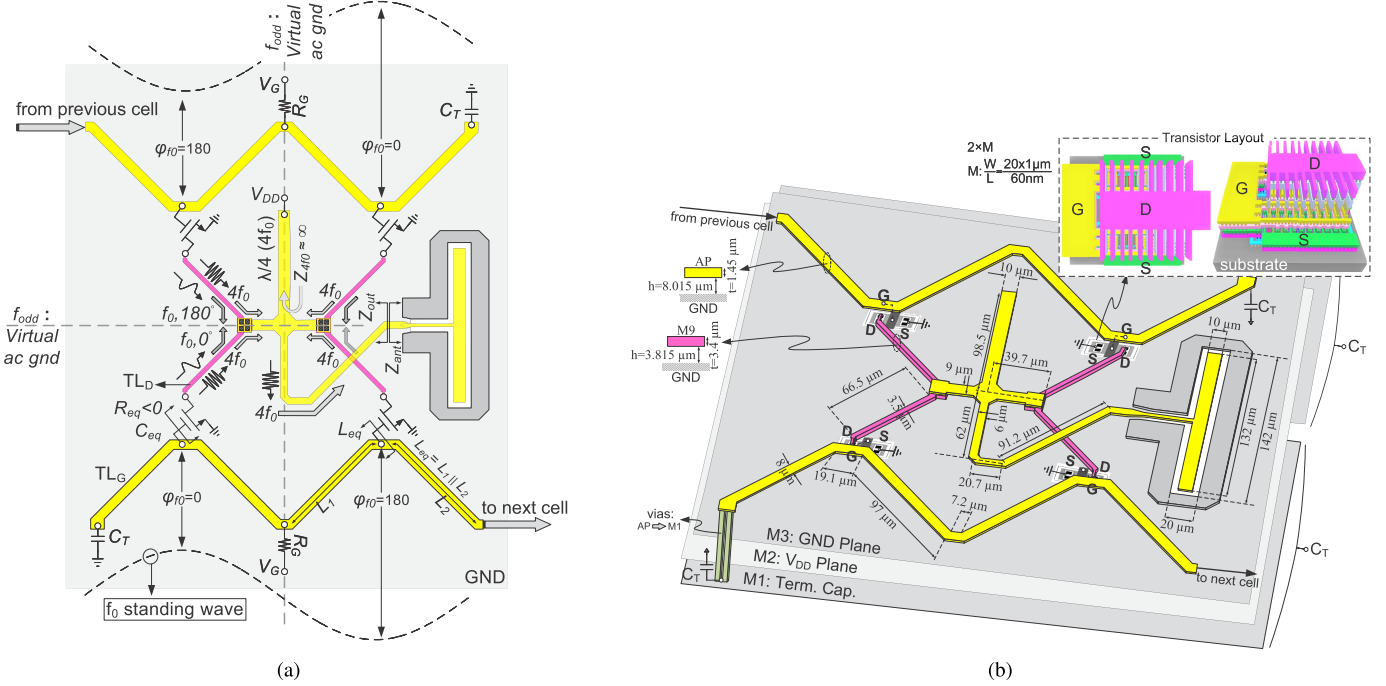


Fig. 2. (a) SWO UCell. (b) Implementation of the UCell including the integrated folded slot antenna.

off-chip power extraction both enable and force us to employ on-chip antennas for direct radiation of the output power. However, there are important challenges in implementing integrated planar antennas. The low-resistivity silicon substrate traps a major part of the radiation energy inside it through excitation of surface waves. This can significantly degrade the radiation efficiency of on-chip antennas [33]–[35]. Several solutions have been proposed and implemented in the literature to address this issue. Using a ground plane to isolate the antenna from the lossy substrate is one possibility [22]–[25]. However, the small thickness of back-end oxide layers limits the performance of these antennas. In this case, directivity (D) and efficiency can be improved by incorporating a superstrate on top of the chip [8], [36]. Alternatively, substrate-thinning can be used to prevent the substrate from supporting the excitation of lossy surface waves [26]. Using a silicon lens is another method for back-side radiation from the chip [5], [6], [19], [29], [30]. Attaching a silicon lens to the substrate significantly improves the directivity as well as increasing the radiation efficiency by suppressing the surface waves in the substrate. Despite its popular use, the radiation behavior of an array in a chip-lens configuration has not been adequately explored.

In this work, we implemented a wideband high-EIRP source by employing a scalable array structure whose dimensions can be extended without introducing extra parasitics or losses to the circuit. SWO unit cells (UCells) are employed as the array building blocks and are coupled together without added passive loss or parasitics in a scalable structure. A varactor-less frequency tuning mechanism is used to extend the circuit bandwidth. The EIRP is increased by both raising the total power that is delivered to the antennas and the array's radiation

gain. P_{rad} is boosted by increasing the size of the array using the proposed scalable structure and directivity is maximized by employing a wideband on-chip antenna with a silicon lens in an optimized radiation setup. We demonstrate in this article that the physical choices for the lens-based radiation setup have a significant impact on the directivity and EIRP of the circuit.

In this article, Section II describes the UCell of the array as well as the employed scalable coupling method and the structure of the implemented array. The design of the integrated antenna and characteristics of the lens-based radiation setup are discussed in Section III. The experimental results of this article are presented in Section IV, and Section V brings this article to a conclusion.

II. ARRAY STRUCTURE AND DESIGN

The implemented array consists of SWO UCells that are coupled together in a continuous and scalable structure with no extra coupling loss and integrated antennas for radiation of the generated coherent THz power. This section describes the UCell of the array circuit as well as the employed scalable coupling scheme.

A. Array's UCell

Fig. 2(a) and (b) shows the schematic and implementation structure of the array's UCell, respectively. It consists of a harmonic SWO and a folded slot antenna for radiation of the extracted fourth harmonic power through the back side of the chip. The operation principle of the UCell's SWO is similar to that described in [32]. However, unlike [32], the UCCells are coupled together in a way that makes it possible to construct a

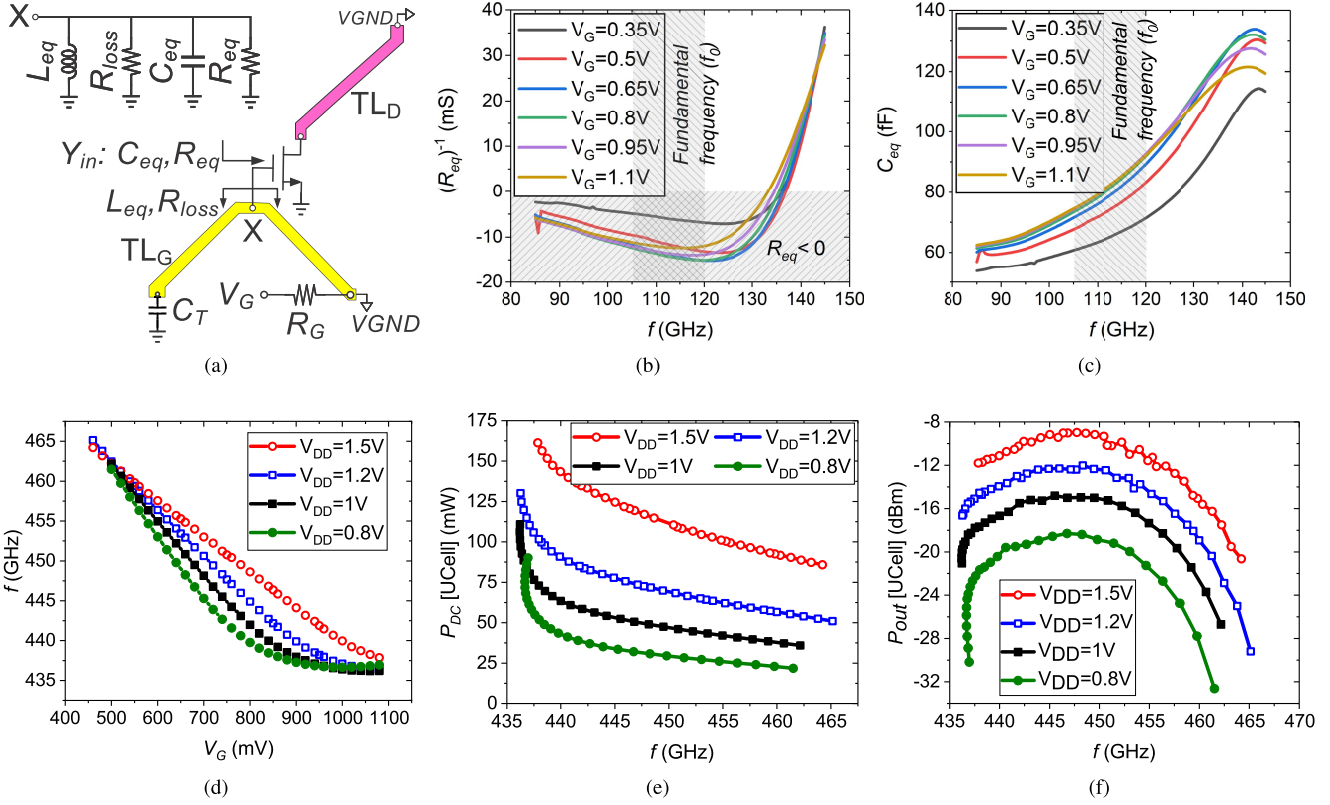


Fig. 3. (a) Equivalent circuit of the UCell at fundamental frequency (f_0), (b) simulated negative resistance $[(R_{eq})^{-1}]$, and (c) simulated capacitance (C_{eq}) at the gate of the transistor. Simulated (d) fourth harmonic frequency, (e) power consumption, and (f) output power of the UCell.

scalable array structure. We will discuss the coupling scheme in detail in Section II-B. Furthermore, the oscillator is designed to maximize the fourth harmonic power radiation through on-chip antennas instead of second harmonic probe-based extraction in [32].

Out-of-phase fundamental frequency (f_0) standing waves are formed on the gate transmission lines (TL_G) which results in systematic cancellation of fundamental frequency power and all its odd harmonics. This creates virtual ground planes across the lines of symmetry in the circuit at f_0 and its odd harmonics. Fig. 3(a) shows the equivalent circuit of the SWO at f_0 . The short-terminated drain transmission line (TL_D) creates an inductive drain impedance. The transistors with inductive drain impedance provide the necessary negative resistance (R_{eq}) for oscillation at their gate terminals. Fig. 3(b) shows the simulated $(R_{eq})^{-1}$ in the SWO circuit. The transistors are placed at the anti-nodes of the TL_G standing waves and therefore experience the maximum oscillation amplitude at their gate terminals. The harmonics of the fundamental frequency are therefore generated through the nonlinearity of the transistors. In addition to loss compensation and harmonic generation, transistors are used as active variable capacitors for frequency tuning in order to avoid the unwanted loss and parasitics of varactors. Looking at the resonance circuit at node X in Fig. 3(a), the negative resistance of the transistor (R_{eq}) cancels the losses in the circuit (modeled here by a lumped resistor R_{loss}) and the frequency of oscillation is determined by the input capacitance of the transistor (C_{eq})

and the inductance of TL_G (L_{eq}). Therefore, the frequency of operation can be altered by changing the gate bias (V_G) of the transistor and therefore varying the capacitor in the oscillator's resonance circuit. Fig. 3(c) shows the simulated C_{eq} for different gate bias levels from 0.35 to 1.1 V in the circuit. It can be seen in Fig. 3(b) that R_{eq} remains negative for this range of V_G values. The V_G bias voltage is applied at the nodes of the standing waves with zero fundamental frequency amplitude, thus avoiding any unwanted loading effect of the bias circuitry on the ac operation of the circuit. We have previously presented a detailed analysis of the operation of the SWO and the employed frequency tuning mechanism for a SiGe HBT implementation in [25].

Due to the out-of-phase formation of standing waves on the top and bottom TL_G , the phases of fundamental frequency oscillation at transistors' gates are either 0° or 180° . This is shown in Fig. 2(a). This means that while the fundamental frequency power and its odd harmonics cancel out, the generated even harmonics are in phase and add up constructively. The desired fourth harmonic ($4f_0$) powers are combined and fed to the on-chip folded slot antenna for radiation. The second harmonic radiation is suppressed by the input matching and radiation efficiency of the antenna at that frequency. The detailed characterization of the integrated antenna is presented in Section III.

Fig. 2(b) shows the implementation detail of the array's UCell. The TL_G and TL_D transmission lines are implemented using top AP metal layer and M9 metal layer microstrips,

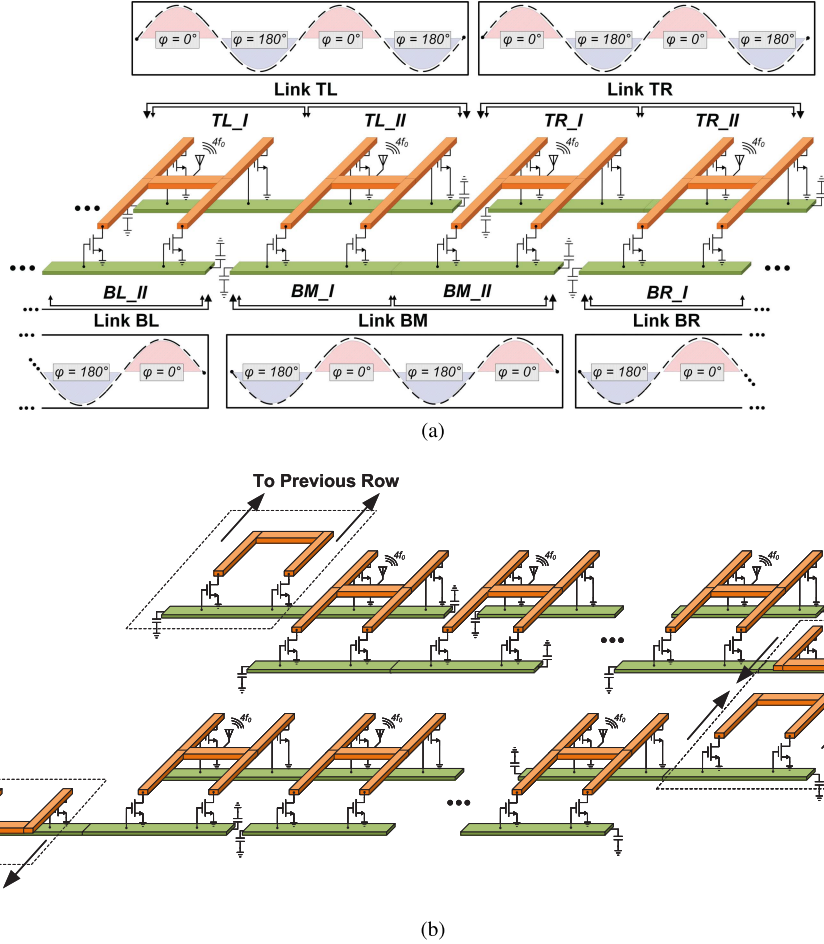


Fig. 4. (a) Coupling scheme and (b) scaling of the array using the proposed method.

respectively. The antenna, its feed line, and the $\lambda/4$ -line (at $4f_0$) that is used to apply the supply voltage (V_{DD}) are implemented by the top AP layer. Universal gnd and V_{DD} planes are implemented using M3 and M2 metal layers, respectively. The top and bottom TL_G transmission lines are terminated on opposite sides by capacitor C_T . Ideally, we require this capacitor to be large enough to create a close-to-short impedance while being insensitive to process variations. An imbalance between C_T magnitudes on opposite sides of TL_G can create an unwanted phase error and reduce the output power. Therefore, the top and bottom C_T are implemented as large M1-M2 parallel-plane capacitors that each occupy half the area underneath the UCell. The UCell circuit is laid out in a way so as to create the necessary space for the integrated antennas between cells while preserving symmetry and minimizing the routing path loss of the output power. The entire structure of the SWO is electromagnetically simulated altogether and used in the design process. Fig. 3(d)–(f) shows the simulated fourth harmonic frequency, power consumption, and output power (delivered to the antenna) of the SWO UCell.

B. Array Structure: Coupling and Scaling

The EIRP of the THz source can be increased by either increasing the transmit power (P_t) generated by the circuit or

increasing the gain (G_t) of the radiation structure since

$$\begin{aligned} \text{EIRP (dBm)} &= P_t (\text{dBm}) + G_t (\text{dB}) \\ &= P_t (\text{dBm}) + D_t (\text{dB}) + e_{\text{rad}} (\text{dB}) \end{aligned} \quad (1)$$

where D_t and e_{rad} are the transmitter's overall directivity and radiation efficiency, respectively. We will discuss our approach to maximizing G_t in detail in Section III. The transmit power (P_t), on the other hand, can be improved by increasing the number of coupled UCells and forming an array of sources that generate in-phase THz power. This coupling also has a desirable effect in reducing the phase noise of each individual oscillator [37]. Oscillators are often coupled together using passive elements. However, these coupling networks come with losses and parasitics that negatively affect the frequency of operation, tuning range, and output power of the UCell. Our approach in this work avoids extra loss and parasitics by using a new continuous and scalable method of extending the array size in 2-D while maintaining coherency of the generated THz power.

Fig. 4(a) illustrates the operation principle of the employed coupling method. Here, the bottom middle link (Link BM) acts as a bridge between the top left and right links (Link TL and Link TR) and maintains $0^\circ/180^\circ$ phase relation between them even though Link TL and Link TR are not directly coupled together. A two-wavelength standing wave is formed on the gate transmission line in Link BM which enforces $0^\circ/180^\circ$

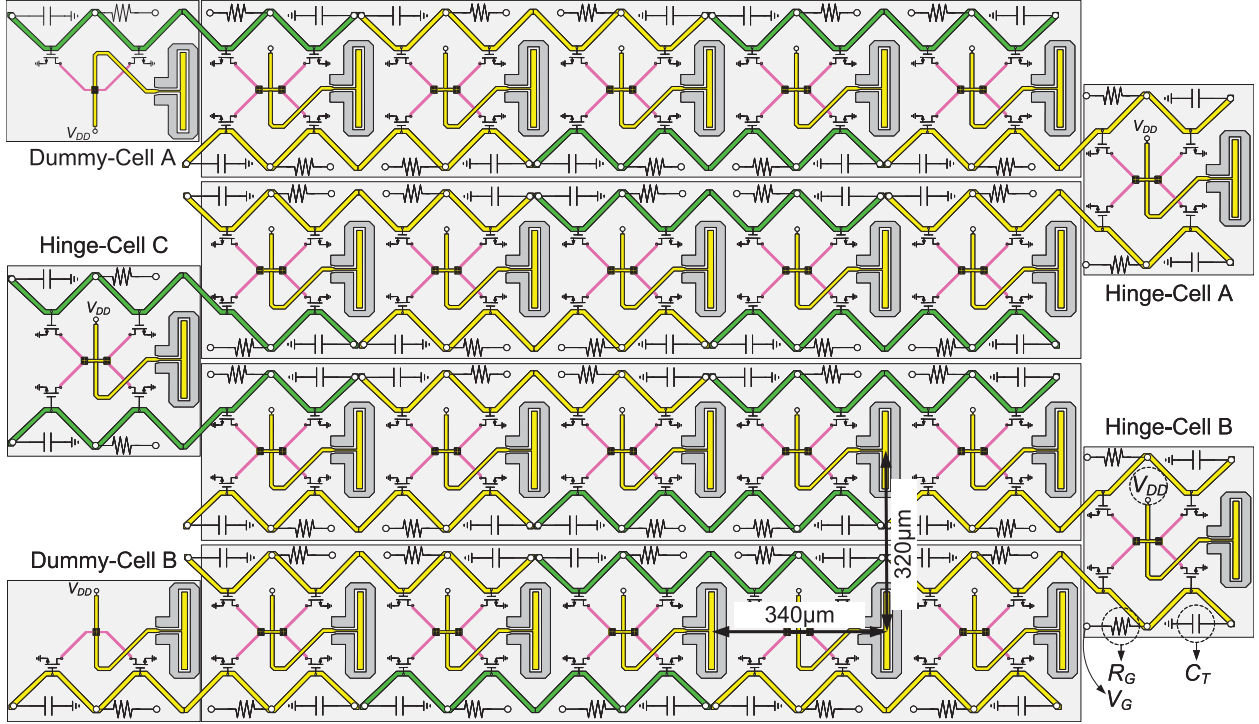


Fig. 5. Full structure of the implemented array.

phase operation on the transistors in Link BM. At the same time, half of Link BM (BM_I) is coupled to Link TL and the other half (BM_II) to Link TR using T_{LD} transmission lines. This ensures that TL_{II} and TR_I are out of phase since BM_I and BM_II have to be out of phase. If we continue with this structure, Link TL and Link TR will, in turn, preserve the same phase relationship between Link BM and its adjacent Links on the left and right sides (Link BL and Link BR), respectively. We can therefore extend the array to our desired size in a row without adding any extra passive elements to or between the UCells.

Since the top and bottom halves of the row are shifted by one wavelength relative to each other, there will be “half-cells” on both sides of the row whose T_{LD} lines are left uncoupled. Therefore, our next step is to extend the size of the array in the second dimension using these “half-cells” as hinges that couple successive rows together. This is shown in Fig. 4(b) where two rows are coupled together using the “hinge” cell on the right. Similarly, other rows can be added before or after these two rows by coupling them to half-cells on the left side of the structure. Therefore, we can scale both the number of columns (by extending the rows) and rows (by coupling multiple rows) in the array to our desired size without adding any coupling loss or parasitics to the circuit and maintain the 0°/180° phase relationship for fundamental frequency and coherent fourth harmonic power generation and radiation.

Fig. 5 shows the full structure of the implemented array. The integrated antennas are placed in the empty spaces that are specifically created for this purpose by laying out both gate and drain transmission lines diagonally. We should point out that this area is sufficiently large for a patch antenna at

0.46 THz as well. Therefore, the folded slot antennas can be potentially replaced by patch antennas in case lens-less front-side radiation is desired instead. The core of the circuit consists of a 4×5 array and “hinge-cells” A, B, and C couple the rows together. “Dummy-cells” A and B are unavoidable at the beginning and end of the continuous structure but will not increase in number regardless of the size of the entire array. Since these dummy cells are not facing another half-cell, the drain transmission lines are coupled together. We do not expect any significant mismatch effect because of these dummy cells.

III. INTEGRATED RADIATION STRUCTURE

Silicon lenses are often used in THz sources to minimize the surface wave losses in the substrate and concentrate the radiated power into narrow beams, thereby increasing the radiation gain and hence EIRP [38], [39]. In this section, we explore the behavior of the on-chip antenna/array and Si lens configuration and present the optimum physical conditions for this radiation mechanism that can maximize EIRP.

A. Single Antenna + Lens Radiation

We have employed folded slot antennas for radiation of the THz power through the substrate and silicon lens. This choice offers several benefits including high directivity that directly increases the EIRP of the source and large bandwidth. Furthermore, the slot structure of the antenna minimizes the negative impact of the necessary local density filling cells on the radiation efficiency of the source. Fig. 6(a) shows the attachment configuration of the silicon lens with radius R_{lens}

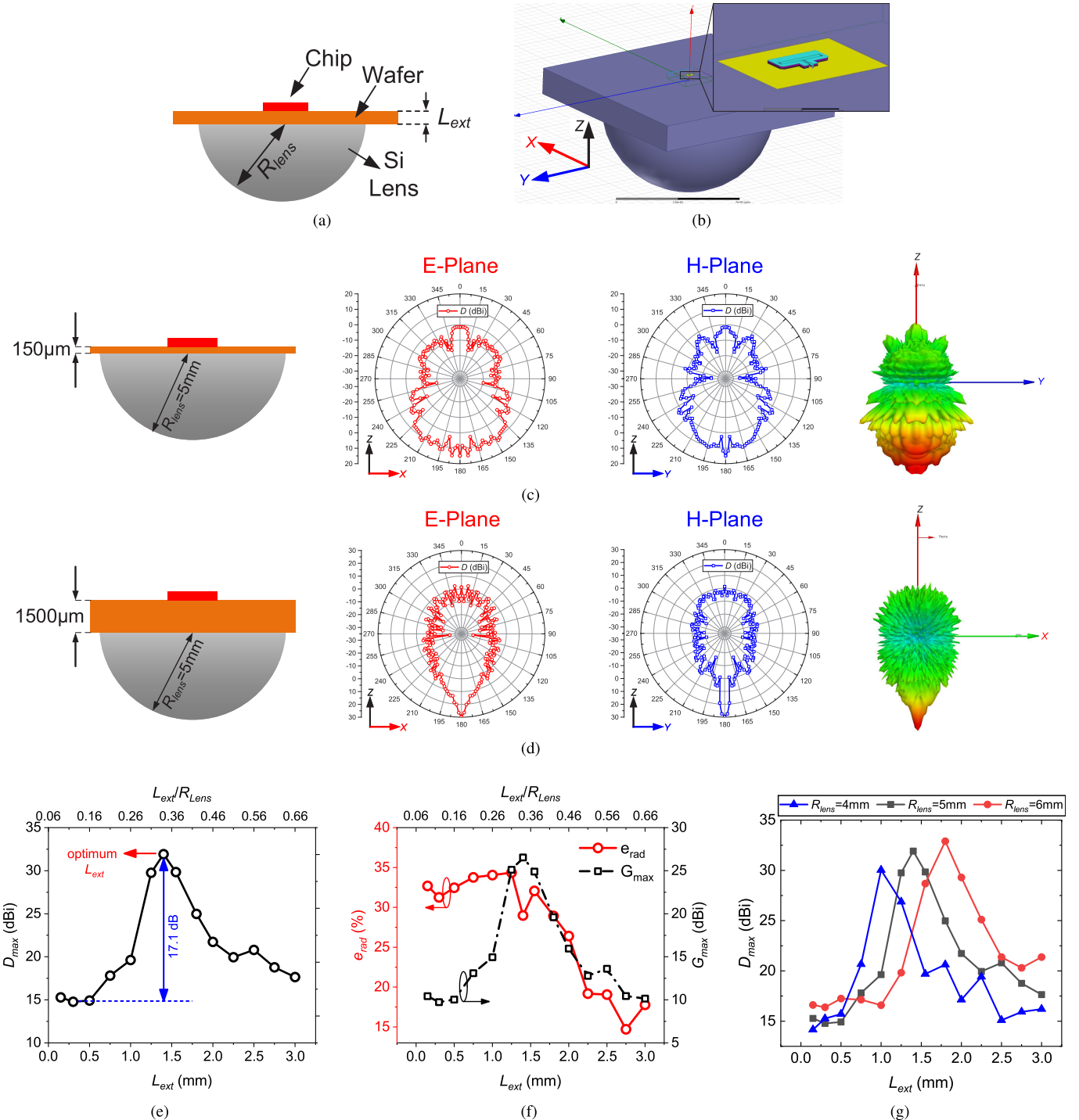


Fig. 6. (a) Substrate radiation through silicon wafer and lens configuration. (b) Antenna simulation in HFSS. (c) Simulated radiation pattern for 150- μm wafer thickness. (d) Simulated radiation pattern for 1500- μm wafer thickness. Simulated (e) D_{\max} (maximum directivity) and (f) e_{rad} (radiation efficiency) of the folded slot antenna for different values of L_{ext} . (g) Simulated D_{\max} versus extension length for different lens sizes.

to the chip's substrate using an intermediate silicon wafer with thickness L_{ext} . The thickness of the wafer acts as an extension length to the lens. In this section, we discuss how the directivity of the antenna can be maximized by proper choices of extension length (L_{ext}) and size of the lens (R_{lens}).

In order to observe the effect of L_{ext} on the radiation behavior of the antenna, we simulated the same folded slot

antenna with identical lenses ($R_{\text{lens}} = 5\text{ mm}$) but with different values of L_{ext} in HFSS 3-D EM simulator [Fig. 6(b)]. Fig. 6(c) and (d) shows the radiation patterns of the antenna for $L_{\text{ext}} = 150\text{ }\mu\text{m}$ and $L_{\text{ext}} = 1.5\text{ mm}$, respectively. We can see that the beam is significantly narrower and more concentrated with $L_{\text{ext}} = 1.5\text{ mm}$ compared to $L_{\text{ext}} = 150\text{ }\mu\text{m}$. This shows that the choice of L_{ext} value has a considerable

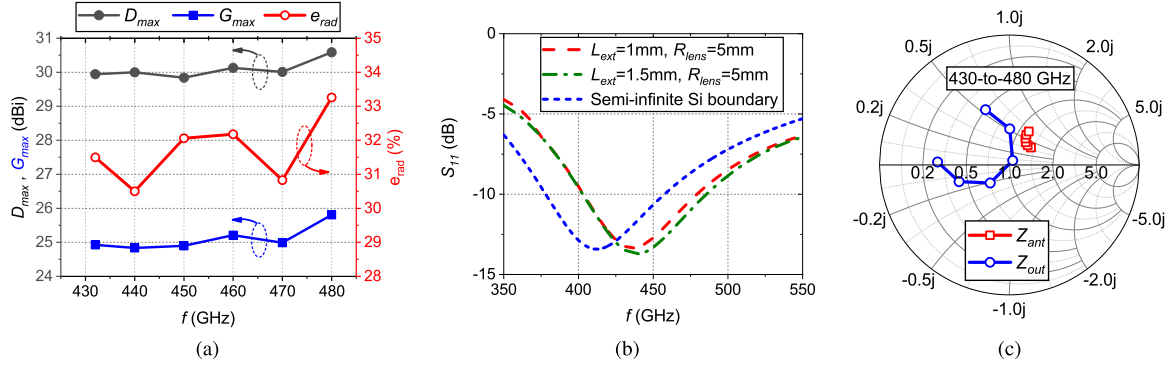


Fig. 7. (a) Simulated maximum directivity (D_{\max}), maximum gain (G_{\max}), and radiation efficiency (e_{rad}) of the employed folded slot antenna versus frequency for $L_{\text{ext}} = 1.5 \text{ mm}$ and $R_{\text{lens}} = 5 \text{ mm}$. (b) Simulated bandwidth (S_{11}) of the antenna. (c) Input impedance of the antenna (Z_{ant}) versus the output impedance of the UCell (Z_{out}) [see Fig. 1(a)] for $L_{\text{ext}} = 1.5 \text{ mm}$ and $R_{\text{lens}} = 5 \text{ mm}$ from 430 to 480 GHz.

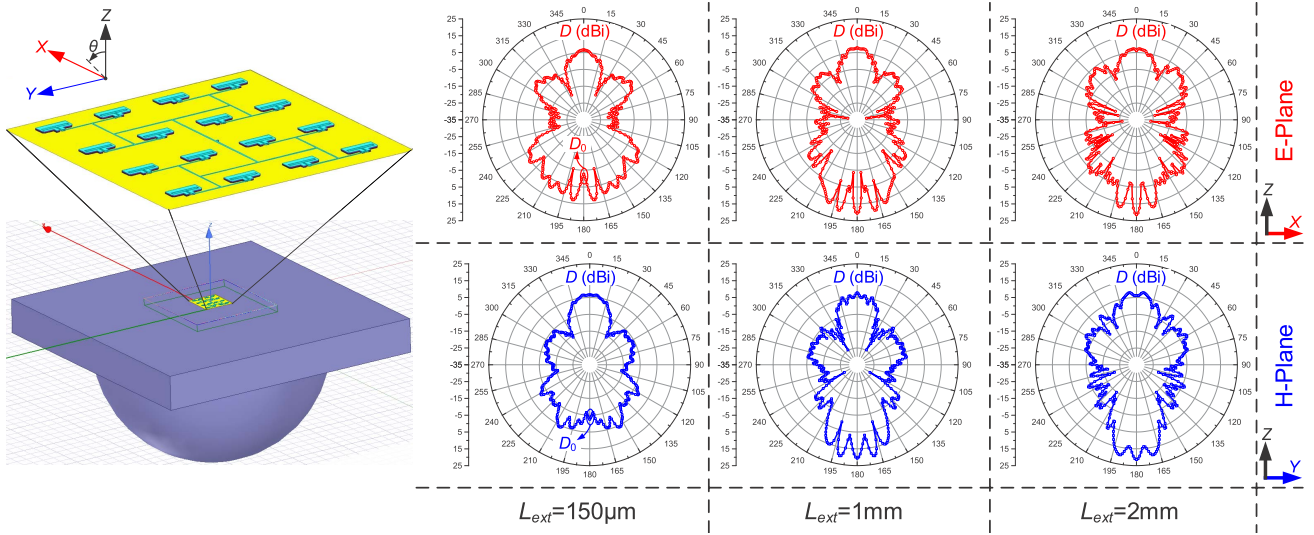


Fig. 8. Simulated radiation patterns of a 4×4 folded slot antenna array with $R_{\text{lens}} = 5 \text{ mm}$ and $L_{\text{ext}} = 150 \mu\text{m}$, 1 mm , and 2 mm .

impact on the directivity and hence EIRP of radiation. It has been shown in [39] that $L_{\text{ext}} \approx 0.36 \times R_{\text{lens}}$ results in maximum directivity. Fig. 6(e) and (f) shows the simulated D_{\max} (maximum directivity), e_{rad} (radiation efficiency), and maximum gain (G_{\max}) of the folded slot antenna for different values of L_{ext} , respectively. A maximum directivity of 31.9 dBi can be achieved with $L_{\text{ext}} = 1.4 \text{ mm}$ and $L_{\text{ext}}/R_{\text{lens}} = 0.34$. It can be seen that there is about 17.1-dB difference between directivity with $L_{\text{ext}} = 1.4 \text{ mm}$ and $L_{\text{ext}} = 0.3 \text{ mm}$.

In addition to the choice of L_{ext} , the size of the lens has an important effect on the radiation characteristic of the antenna. To explore the impact of the lens size, we simulated the folded slot antenna with three different lens sizes while sweeping L_{ext} for each one of them. Fig. 6(g) shows the simulated maximum radiation directivity (D_{\max}) versus L_{ext} for lens radii of 4, 5, and 6 mm. It can be seen that the maximum directivity increases with the lens radius. Furthermore, the optimum value of L_{ext} changes with the lens size as well. This is consistent with our expectation of best L_{ext} occurring at a constant $L_{\text{ext}}/R_{\text{lens}}$. Based on the presented results, we can conclude that the directivity and EIRP of the source can be increased

by using a larger lens while choosing the optimum L_{ext} based on the employed lens size.

As shown in Fig. 3(d), the UCell is capable of providing ~ 30 GHz of tuning range and therefore the antenna behavior as a function of frequency is of interest. Fig. 7(a) shows the simulated maximum gain and directivity as well as radiation efficiency of the antenna as a function of frequency for $L_{\text{ext}} = 1.5 \text{ mm}$ and $R_{\text{lens}} = 5 \text{ mm}$. The value of L_{ext} is chosen to be 1.5 mm instead of the optimum value of 1.4 mm since we had access to 0.5-mm-thick wafers during the measurement. Fig. 7(b) shows the input matching of the antenna with S_{11} below -10 dB within the bandwidth of the circuit. The simulation results presented in Fig. 7 are based on the simulation setup shown in Fig. 6(b). Modeling the Si wafer and lens as a semi-infinite silicon boundary condition underneath the chip substrate can reduce the simulation time and speed up the design process. However, the impedance simulation results deviate from the more realistic setup as shown in Fig. 7(b). Furthermore, the semi-infinite boundary condition predicts the radiation efficiency to be close to 50%, while the more accurate simulation in Fig. 7(a) shows the

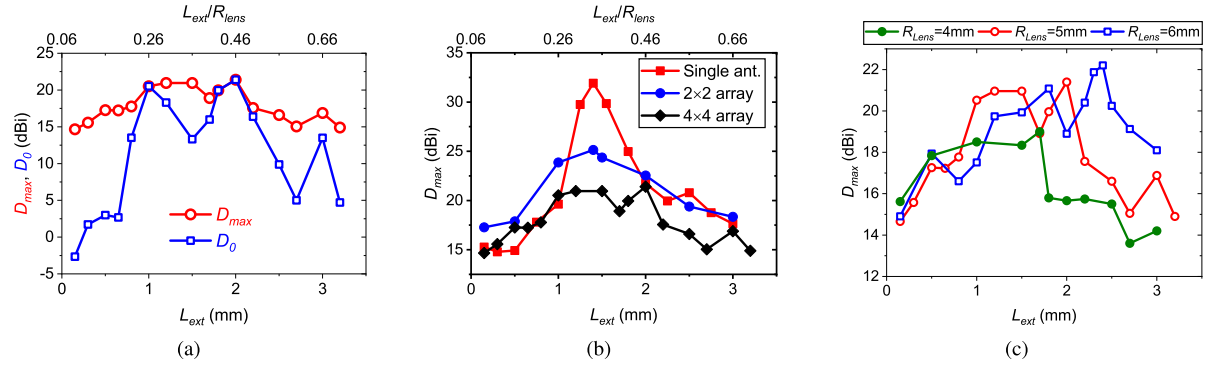


Fig. 9. (a) Simulated radiation directivity for the 4×4 antenna array versus L_{ext} with $R_{\text{lens}} = 5$ mm. (b) D_{\max} of a single antenna, a 2×2 and a 4×4 array with $R_{\text{lens}} = 5$ mm. (c) Simulated maximum directivity (D_{\max}) for the 4×4 antenna array versus L_{ext} for $R_{\text{lens}} = 4, 5$, and 6 mm.

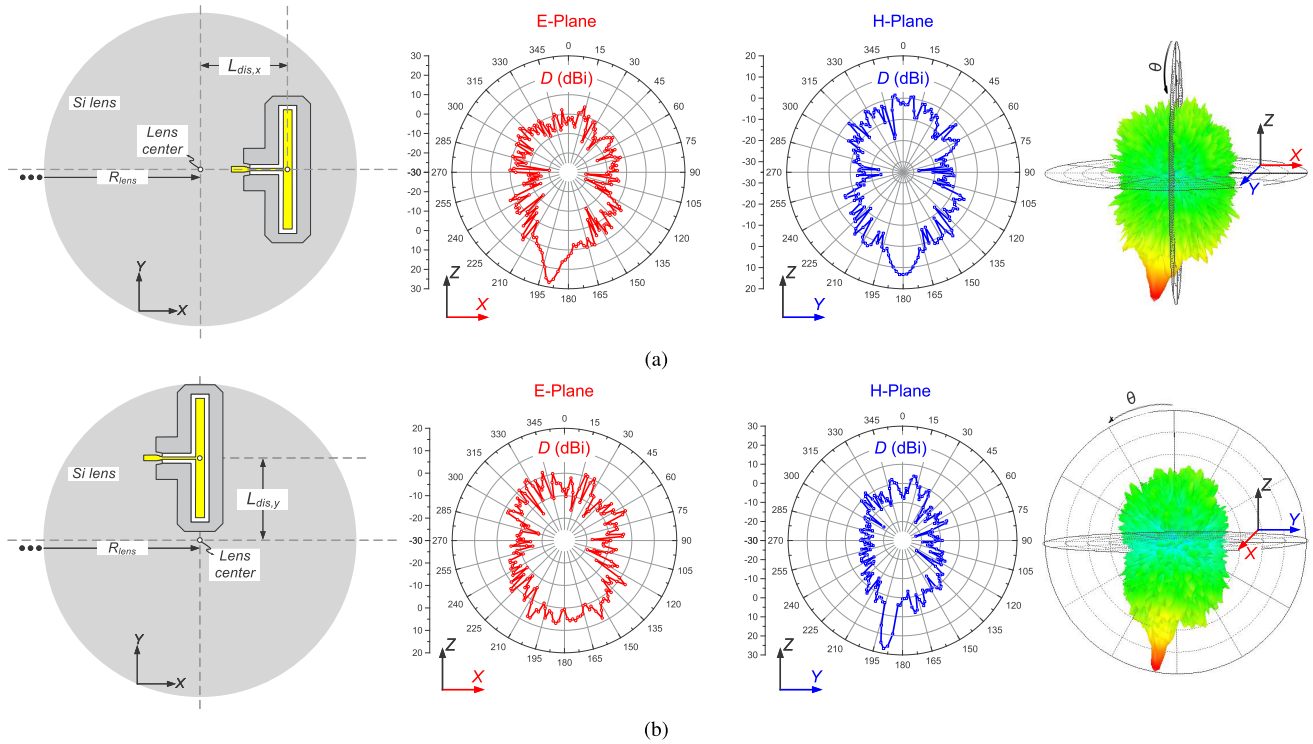


Fig. 10. Simulated radiation patterns of the folded slot antenna with $L_{\text{ext}} = 1.5$ mm and $R_{\text{lens}} = 5$ mm when it is displaced from the center of the lens by (a) $L_{\text{dis},x} = 340 \mu\text{m}$ in the X -direction and (b) $L_{\text{dis},y} = 320 \mu\text{m}$ in the Y -direction.

efficiency to be roughly 32%. The output impedance of the UCell [Z_{out} in Fig. 2(a)] is also matched to 50Ω and is shown in Fig. 7(c) versus the antenna impedance (Z_{ant}) for $L_{\text{ext}} = 1.5$ mm and $R_{\text{lens}} = 5$ mm from 430 to 480 GHz.

B. Antenna Array + Lens Radiation

Even though many works in the literature use Si lens for THz array radiation [3], [5]–[7], [28], [43], the radiation characteristics of an array-lens configuration have rarely been explored. In order to maintain the generality of results, we present our analysis here based on a more conventional 4×4 symmetrical array. This array consists of the same folded slot antennas with the same horizontal and vertical antenna spacings as the implemented array. Similar to the

case of a single antenna, we start by looking at the effect of L_{ext} on the radiation behavior of the array. Fig. 8 shows the radiation patterns of the array with a 5-mm-radius lens and for three different values of extension lengths. As expected, similar to the single antenna, the choice of extension length plays an important role in determining the directivity and therefore EIRP of the source. Fig. 9(a) shows the maximum directivity (D_{\max}) and directivity at $\theta = 180^\circ$ (see Fig. 8) along the lens's center axis (D_0) for this 4×4 array for different values of L_{ext} . The maximum directivity is equal to 21.4 dB at $L_{\text{ext}} = 2$ mm. Fig. 9(b) compares the D_{\max} for the scenarios of a single antenna, a 2×2 and a 4×4 array. We can see that the variations of D_{\max} with L_{ext} and the peak value of D_{\max} decrease as we extend the array. However, D_{\max} can still be increased by 6.7 dB by simply changing L_{ext} from 150

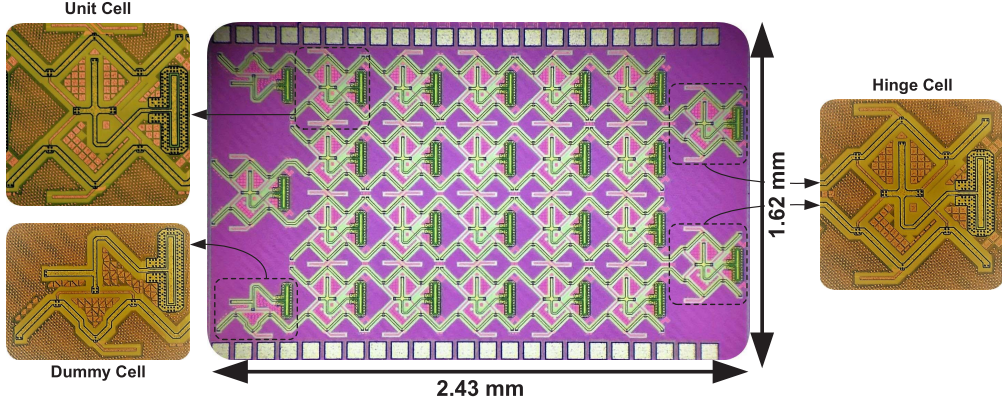


Fig. 11. Die photograph of the implemented prototype chip.

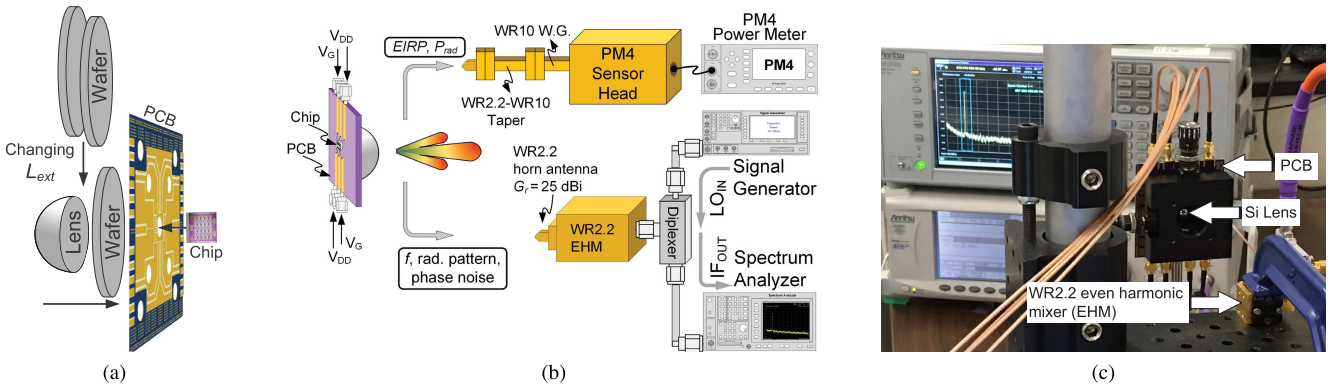


Fig. 12. (a) Assembly configuration of the measured prototype systems. A 0.5-mm-thick wafer is attached to the back side of the PCB, and the chip is attached to it from the front side of the PCB through the hole in the middle of the board. L_{ext} is altered by changing the number of wafers between the Si lens and the wafer that is attached to the PCB. (b) Measurement setup that was used for the characterization of the chip's performance. (c) Snapshot of the setup during the process of lens alignment using an XY translation mount device.

μm to 2 mm in a 4×4 array. We can also see in Fig. 9(a) that for most of the values of L_{ext} , D_0 is smaller than D_{\max} . This means that if the lens is aligned with the center of the array footprint, the peak of the radiated beam will no longer be at $\theta = 180^\circ$. This scenario is clearly shown in the case of $L_{\text{ext}} = 150 \mu\text{m}$ in Fig. 8.

The maximum array directivity (D_{\max}) of the 4×4 array with $R_{\text{lens}} = 5 \text{ mm}$ and $L_{\text{ext}} = 2 \text{ mm}$ is 21.4 dBi, while D_{\max} of a single antenna with the same R_{lens} and $L_{\text{ext}} = 1.4 \text{ mm}$ is 31.9 dBi. In other words, counter-intuitively, the radiation gain decreases when the lens is fed by an array of antennas rather than a single one. In a conventional lens-less radiation setup, the directivity would increase by $10\log(N)$, where N is the number of array elements. Furthermore, a similar increase in the total transmit power (P_t) gives a net increase of $20\log(N)$ to the EIRP. In this case, however, directivity has dropped by 10.5 dB instead even though the number of antennas and the total transmit power is increased by 12 dB. In other words, we have increased P_t at the expense of array gain and we, therefore, do not observe the double boosting effects of array formation on both power and gain. The maximum radiation gain of the 4×4 folded slot antenna array with lens at $L_{\text{ext}} = 2 \text{ mm}$ and $R_{\text{lens}} = 5 \text{ mm}$ is about 15.6 dBi.

A designed 4×4 patch antenna array with the necessary local metal fillings underneath the antenna has a maximum gain of about 12.4 dBi. Therefore, employing a lens-coupled radiation structure is still beneficial despite the drop in the directivity. Furthermore, we go on to demonstrate here that the magnitude of this drop in directivity can be reduced by increasing the size of the lens.

The reason for the drop in the gain of the array compared to a single antenna is rooted in the positions of array elements relative to the center of the lens. The simulation results presented in Section III-A were all based on the assumption that the center of the antenna is perfectly aligned to the center of the lens. In an array, however, even if the lens is perfectly aligned with the center of the array's footprint, most of the array elements would have an off-axis displacement (L_{dis}) relative to the lens center. Therefore, if we look at each antenna in the array individually, they would have different radiation patterns from each other and from the ideal aligned case. The effect of this displacement for a single antenna is studied in [40] and it has been shown that this misalignment results in steering of the radiation beam. This phenomenon has been intentionally exploited in [41] to perform beam steering by mechanically moving the lens relative to the source antenna.

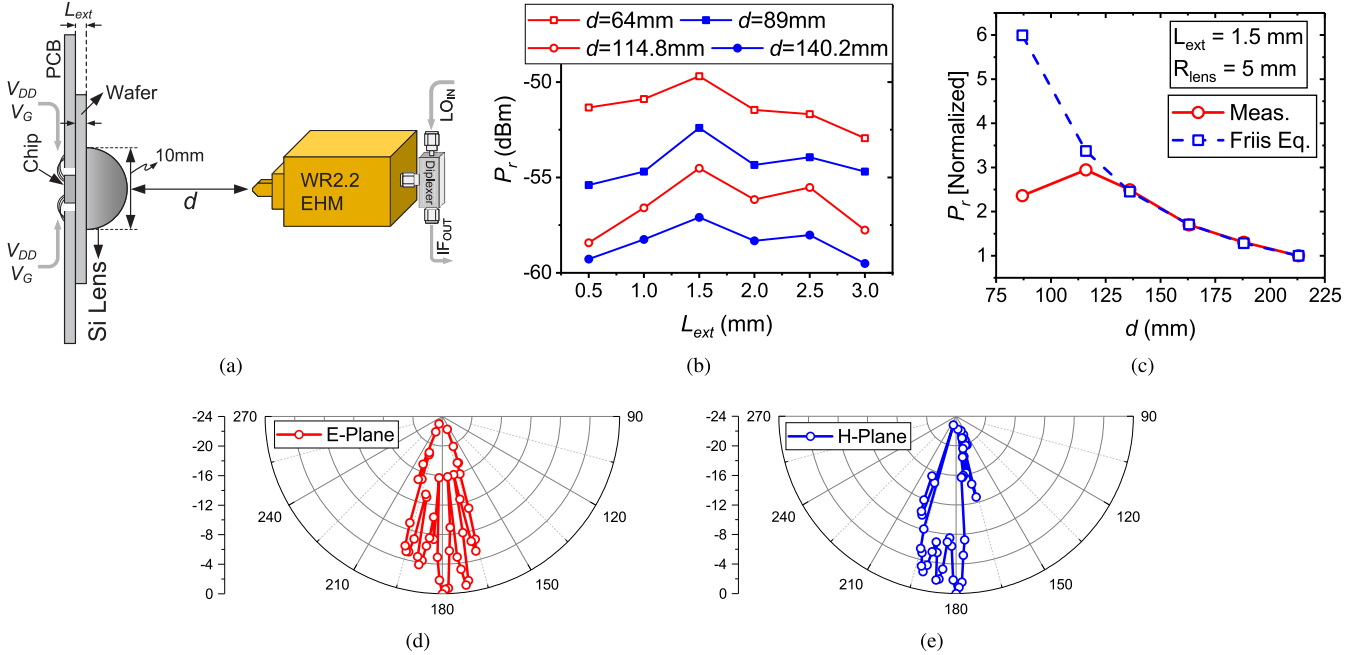


Fig. 13. (a) Measurement setup used for finding the optimum value of L_{ext} , far-field distance, and characterizing the radiation patterns of the source with a $R_{lens} = 5$ mm Si lens. (b) Received power levels for different values of L_{ext} at increasing distances, showing maximum level at far-field for $L_{ext} = 1.5$ mm. (c) Normalized received power levels for $R_{lens} = 5$ mm and $L_{ext} = 1.5$ mm versus distance and compared to Friis transmission equation, showing a far-field distance of approximately 14 cm. Measured radiation patterns of the array source in (d) E - and (e) H -planes for $R_{lens} = 5$ mm, $L_{ext} = 1.5$ mm, and $d = 14$ cm.

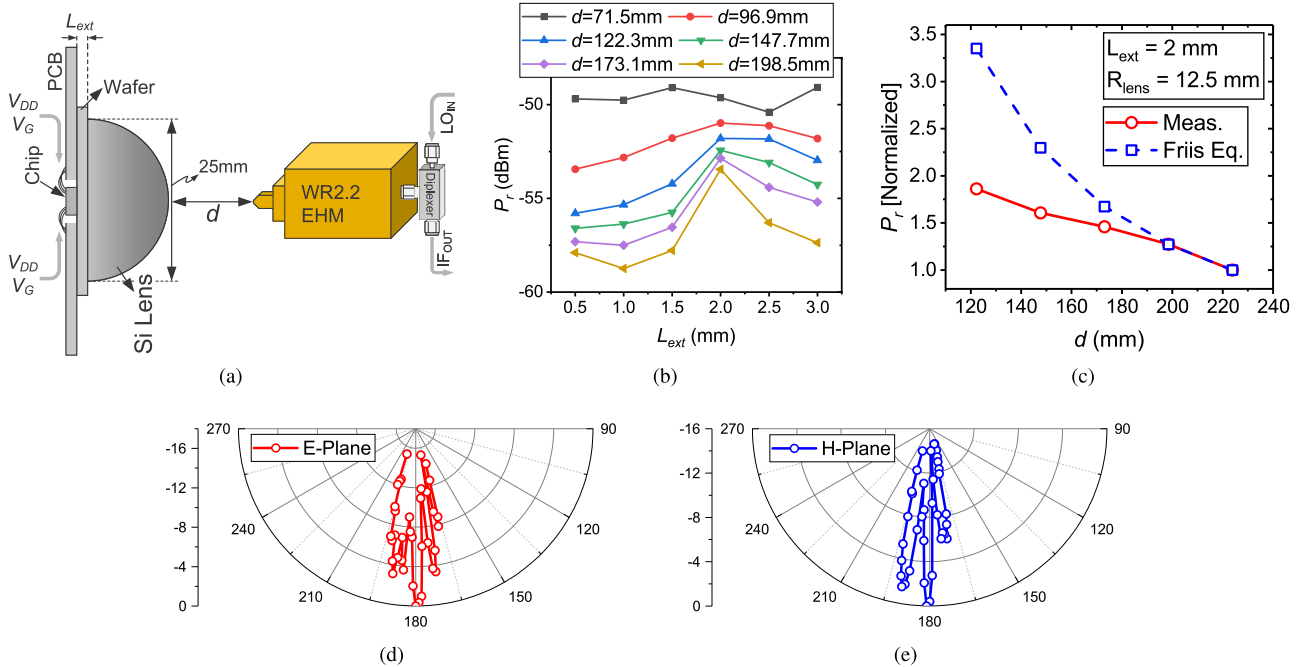


Fig. 14. (a) Measurement setup used for finding the optimum value of L_{ext} , far-field distance, and characterizing the radiation patterns of the source with a $R_{lens} = 12.5$ mm Si lens. (b) Received power levels for different values of L_{ext} at increasing distances, showing maximum level at far-field for $L_{ext} = 2$ mm. (c) Normalized received power levels for $R_{lens} = 12.5$ mm and $L_{ext} = 2$ mm versus distance and compared to Friis transmission equation, showing a far-field distance of approximately 20 cm. Measured radiation patterns of the array source in (d) E - and (e) H -planes for $R_{lens} = 12.5$ mm, $L_{ext} = 2$ mm, and $d = 20$ cm.

Here, we have studied the effect of this behavior on the gain and of a lens-based antenna array. Fig. 10 shows the deviation of radiation beam from the center when the antenna is misaligned

by $L_{dis,x} = 340 \mu\text{m}$ and $L_{dis,y} = 320 \mu\text{m}$ in the x - and y -directions, respectively. The 340- and 320- μm distances are also the antenna spacings in the simulated and implemented

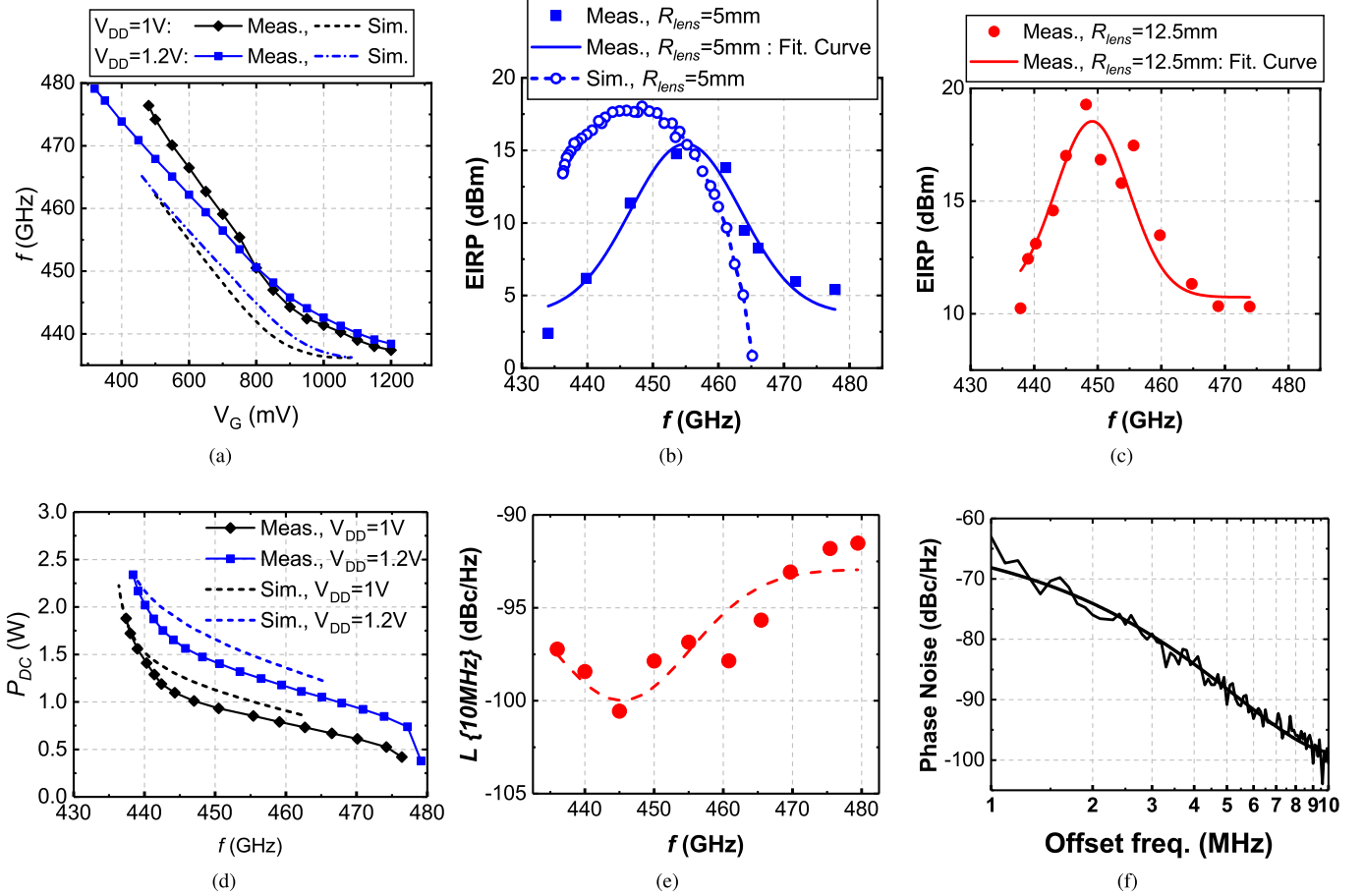


Fig. 15. (a) Measured and simulated frequency of the source. (b) Measured and simulated EIRP for $R_{lens} = 5$ mm. The simulation results are estimated based on the simulated values for the output power of a single UCell, the radiation efficiency of the folded slot antenna, and the directivity of a 4×4 array with $L_{ext} = 1.5$ mm and $R_{lens} = 5$ mm. (c) Measured EIRP for $R_{lens} = 12.5$ mm, (d) measured and simulated power consumption, (e) measured phase noise at 10-MHz offset frequency within the tuning range of the circuit, and (f) measured phase noise spectrum at 445 GHz.

antenna array. It can be seen that the beam steers away from the center axis in the E - and H -planes as the antenna is misplaced in the x - and y -directions, respectively. The radiation patterns of the antennas that are further away from the center of the array experience even larger deviation from the center. Therefore, different antennas in the array are radiating the power in different directions. This behavior has an important and undesirable effect on the maximum directivity and EIRP of an array source with a lens. The radiation pattern of the array is determined by the superposition of radiation patterns of individual antennas with different displacements relative to the center of the lens. So, unlike a lens-less array, the gain from each antenna is not maximum at $\theta = 180^\circ$. Therefore, not only the array directivity does not increase with $10\log(N)$ but also it drops compared to the single-antenna case. This phenomenon is inevitable in a lens-array setup. However, we expect that its effect can be minimized by increasing the lens size (R_{lens}) since the steering angle of an individual antenna is directly related to its relative displacement L_{dis}/R_{lens} [40]. In order to verify this, we simulated the folded slot antenna for three different lens sizes. The result is shown in Fig. 9(c) with $D_{max} = 19$, 21.4, and 22.2 dBi for $R_{lens} = 4$, 5, and 6 mm, respectively. The feasibility of simulation of larger lens

sizes is restricted by the available processing power. However, we can conclude from Fig. 9(c) that using a larger Si lens can increase the EIRP of the source by increasing the maximum directivity of a single antenna [as shown in Fig. 6(g)] and also minimizing the unwanted steering due to the misalignment of array elements with the lens.

To summarize, the wrong choice of L_{ext} can easily result in much lower EIRP than potentially possible from the same circuit. This is particularly significant since power generation at mm-wave/THz spectrum is quite costly. Furthermore, increasing the size of the array without increasing the size of the lens accordingly can actually be counter-productive for EIRP, which would mean a larger chip area and higher power consumption with no or even negative impact on the performance.

IV. EXPERIMENTAL RESULTS

The chip prototype of the array source was fabricated through a 65-nm CMOS process with $f_{max} = 340$ GHz. Fig. 11 shows the chip photograph of the entire array as well as magnified views of the UCell, hinge cell, and dummy cell. The circuit occupies a total area of 2.43×1.62 mm 2 .

TABLE I
COMPARISON WITH THE STATE OF THE ART

	Array Size	Structure	Radiation	f_c (GHz)	Freq. Tuning Range (%)	Beam Steering (°)	P_{rad} (dBm)	EIRP (dBm)	P_{DC} (W)	DC-to-THz Efficiency (%)	$L\{X\} \text{ MHz}$ (dBc/Hz)	Area (mm ²)	Technology (f_{max})
This Work	25	Continuous Coupled Osc.	Folded Slot Ant. + Si Lens	459	8.9 ¹	0	-2.1	14.7	1.47 ²	0.042	-100.6 (10 MHz)	3.94	65nm CMOS (340GHz)
			$R_{lens}=5 \text{ mm}$				-1.8	19.3		0.045			
JSSC19 [24]	2×2	Coupled Osc.	Patch Ant.	344	15.1	128/53	-6.8	4.9	0.45 ³	0.046	-93.1 (10 MHz)	1.2	130nm SiGe (215GHz)
TMTT18 [25]	1×4	Continuous Coupled Osc.	Patch Ant.	342	5.9	0	-10.5	1.2	0.425	0.021	-98.2 (10 MHz)	1.33	130nm SiGe (215GHz)
JSSC19 [17]	1×4	Ref. Ext. Source ⁴ + ILO Chain	Patch Ant.	531.5	0.9	60	-12	2.3	0.26	0.024	N/A	2.5	40nm CMOS (300GHz)
TMTT16 [18]	1×8	Ext. Power ⁵ + Multiplier	Patch Ant. + Quartz Superstrate	390	10.3 ⁶	75	-7	8	1.5	0.013	N/A	10.5	45nm SOI CMOS (260GHz)
JSSC15 [22]	4×4	Coupled Osc.	Patch Ant.	338	2.1	45/50	-0.9	17	1.54	0.053	-93 (1 MHz)	3.9	65nm CMOS (250GHz)
JSSC12 [26]	4×4	Ref. Int. Source + Mult. + ILO	DAR ⁷ + Subs. Thinning	280	3.2	80/80	-7.2	9.4	0.81	0.0235	N/A	7.2	45nm SOI CMOS (N/A)
JSSC15 [6]	4×4	Coupled Osc. + PLL	Folded Slot + Si Lens	317	N/A	0	0.9	13.9	0.61	0.2	-79 (1 MHz)	2.1	130nm SiGe (280 GHz)
JSSC13 [5]	8-ant.	Coupled Osc.	Slot Ant. + Si Lens				5.2	22.5		0.54			
ISSCC16 [20]	2×3	Wireless Injection Lock	Ring Ant.	296	2.4	0	5.4	22	0.067	5.1	N/A	2.22	65nm CMOS (N/A)
TMTT13 [21]	3×3	Coupled Osc.	Loop Ant.	265	N/A	0	N/A	-6.6	0.092	N/A	-89.3 (1 MHz)	1.56	65nm CMOS (N/A)
RFIC18 [42]	5×6	Manual Gate Voltage Tuning	Loop Ant.	280	4.11	0	9	24.1	0.421	1.88	N/A	2.1	65nm CMOS (N/A)
JSSC18 [43]	91	Coupled Osc.	Dipole Slot Ant. + Si Lens	1010	0.5	0	-10.9	13.1	1.1	0.007	N/A	1	130nm SiGe (450 GHz)
JSSC16 [29]	1	Single Source + PLL	Ring Ant. + Si Lens	553	3.8	0	-27	N/A	0.172	0.001	-85 (10 MHz)	2.79	65nm CMOS (240 GHz)
RFIC17 [19]	1	Osc. + Multiplier	Circular Slot Ant. + Si Lens	431	2.55	0	-6.8	15	0.164	0.13	-89 (10 MHz)	0.19	130nm SiGe (450 GHz)
EuMIC15 [30]	1	Single Source Osc.	Slot Ant. + Si Lens	490	N/A	0	-14.2	N/A	0.065	0.06	N/A	0.29	130nm SiGe (360 GHz)
TTST18 [44]	1	Osc. + Multiplier	Dielectric Lens Ant.	540	5.9	0	-22	-7.4	0.019	0.033	N/A	0.12	28nm CMOS (N/A)

¹ 438.4-to-479.1 GHz³ 0.45 W at 344 GHz, 0.31-to-0.64 W for 370-to-318 GHz⁵ 10 dBm input power at 100 GHz⁷ Distributed Active Radiator (DAR)² 1.18 W at 459 GHz (center frequency), 1.47 W at 448 GHz (peak-EIRP), 2.34 W at 438.4 W and 0.38 W at 479.1 GHz (bandwidth boundaries)⁴ 88.5 GHz input for phase shifting and injection locking⁶ 3-dB power bandwidth when changing input frequency

Separate universal gnd and supply voltage (V_{DD}) planes cover the entire area underneath the chip using M3 and M2 metal layers, respectively. Moreover, a large number of gnd and supply pads (22 pads for each) are symmetrically placed on top and bottom of the chip to further minimize any undesired effect due to bias mismatch between array cells. The gate bias routing is done symmetrically underneath the gnd and V_{DD} planes using the M1 metal layer so as to minimize any undesired coupling to the passive structures of the array cells.

Fig. 12(a) shows the configuration of the measured prototype systems. A 500-μm-thick undoped high-resistivity ($>15 \text{ K}\Omega \cdot \text{cm}$) silicon wafer with 1 in diameter was glued to the back side of an FR4 PCB with a hole in the middle. The chip was then attached to the wafer inside the hole area of the board. Therefore, the front side of the chip is exposed and gate bias and supply voltages are applied to the circuit through bond wires that connect the PCB tracks to the chip's pads. A high-resistivity hemispherical silicon lens is attached to the other side of the wafer. Fig. 12(b) shows the measurement setup of the chip. On the receiver side, a VDI WR2.2 horn antenna captures the beam followed by an Erickson power meter for EIRP and radiated power (P_{rad}) measurement and a VDI WR2.2 even harmonic mixer (EHM) for measuring the

frequency, phase noise, and radiation patterns of the circuit. Fig. 12(c) shows a snapshot of the measurement setup where the lens is placed inside the XY translation mount device and its position is adjusted based on the received power by the EHM.

In order to experimentally find the best choice for L_{ext} , we altered L_{ext} by adding 500-μm-thick wafers between the Si lens and the original wafer that is attached to the board. For each value of L_{ext} , we re-adjusted the lens position to maximize the received power by the EHM and recorded its magnitude for different values of L_{ext} for comparison. We carried out this procedure for two separate lenses with $R_{lens} = 5 \text{ mm}$ and $R_{lens} = 12.5 \text{ mm}$. For $R_{lens} = 5 \text{ mm}$ [Fig. 13(a)], the received power levels versus L_{ext} for different distances (d) between the transmitter chip and the receiver antenna are shown in Fig. 13(b). It can be seen that maximum power is received with $L_{ext} = 1.5 \text{ mm}$. We therefore carried out the rest of the measurements for $R_{lens} = 5 \text{ mm}$ with this choice of L_{ext} . We then proceeded to measure the received power versus d in order to find the appropriate far-field distance by comparing its variation with the Friis transmission equation. The measured normalized received power versus distance is shown in Fig. 13(c). It shows that the radiated power

follows the Friis equation from about $d = 14$ cm. Therefore, we used this distance for far-field measurements of the array, including characterizations of radiation patterns, EIRP, and P_{rad} . Fig. 13(d) and (e) shows the measured radiation patterns of the array at a 14 cm distance in the E - and H -planes, respectively.

Following a similar procedure for $R_{\text{lens}} = 12.5$ mm [Fig. 14(a)], we found the optimum value for L_{ext} to be 2 mm as shown in Fig. 14(b) and the far-field distance to be about 20 cm as shown in Fig. 14(c). Fig. 14(d) and (e) shows the measured radiation patterns of the array with $R_{\text{lens}} = 12.5$ mm at 20 cm distance in the E - and H -planes, respectively.

Fig. 15(a) shows the measured and simulated frequency of the radiated power for 1- and 1.2-V supply voltages. The frequency can be altered from 438.4 to 479.1 GHz with a 1.2-V supply which is equivalent to 8.9% tuning range. The EIRP of the circuit is measured using the received power by the power meter and based on Friis equation and is shown in Fig. 15(b) and (c) for $R_{\text{lens}} = 5$ mm and $R_{\text{lens}} = 12.5$ mm with maximum levels of 14.8 dBm at 453 GHz and 19.3 dBm at 448 GHz, respectively. Fig. 15(b) also shows an estimation of the expected EIRP based on the simulated values for output power of a single UCell, the radiation efficiency of the folded slot antenna, and the directivity of a 4×4 array with $L_{\text{ext}} = 1.5$ mm and $R_{\text{lens}} = 5$ mm. We can see that the measured results follow the simulated values closely. Based on the measured radiation patterns of the array in Figs. 13 and 14, the directivity, calculated using a similar approach as in [5], is 16.8 and 21.14 dBi for $R_{\text{lens}} = 5$ mm and $R_{\text{lens}} = 12.5$ mm, respectively. The radiated power (P_{rad}) can then be calculated based on the measured EIRP and directivity [$P_{\text{rad}} (\text{dBm}) = \text{EIRP} (\text{dBm}) - \text{Directivity} (\text{dB})$]. The peak values of P_{rad} are -2.1 and -1.8 dBm for $R_{\text{lens}} = 5$ mm and $R_{\text{lens}} = 12.5$ mm, respectively.

The measured power consumption of the circuit across the bandwidth of operation is shown in Fig. 15(d). The chip consumes between 380 mW at 479.1 GHz and 2.34 W at 438.4 GHz from a 1.2-V supply. The power consumption at 448 GHz with maximum EIRP is 1.47 W. Fig. 15(e) shows the measured phase noise of the radiated power within the bandwidth of the circuit at 10-MHz offset frequency. The minimum phase noise level is -100.6 dBc/Hz at 445 GHz and Fig. 15(f) shows the measured spectrum of the phase noise at this frequency.

Table I presents a performance summary of this article and a comparison with the state of the art and shows that we were able to simultaneously achieve large bandwidth and high EIRP well above f_{max} in a fully integrated silicon implementation. To our knowledge, this article has the highest EIRP and radiated power (P_{rad}) and the largest frequency tuning range among fully integrated silicon-based coherent sources above 350 GHz.

V. CONCLUSION

In this article, we presented a 0.46-THz fully integrated radiator array circuit in a 65-nm CMOS process. We used a scalable structure to extend the size of the array. This structure consists of coupled standing wave harmonic oscillators without

extra loss and parasitics due to the coupling of oscillators. The radiation directivity is maximized by employing an optimized lens integrated radiation setup and a wide bandwidth of operation was achieved using a varactor-less frequency tuning method. As a result, to the best of our knowledge, the implemented circuit demonstrates the highest EIRP and radiated power (P_{rad}) and the largest frequency tuning range among fully integrated silicon-based coherent sources above 350 GHz.

REFERENCES

- [1] P. H. Siegel, "Terahertz technology," *IEEE Trans. Microw. Theory Techn.*, vol. 50, no. 3, pp. 910–928, Mar. 2002.
- [2] S. P. Voinigescu, S. Shopov, J. Bateman, H. Farooq, J. Hoffman, and K. Vasilakopoulos, "Silicon millimeter-wave, terahertz, and high-speed fiber-optic device and benchmark circuit scaling through the 2030 ITRS horizon," *Proc. IEEE*, vol. 105, no. 6, pp. 1087–1104, Jun. 2017.
- [3] C. Wang and R. Han, "Dual-terahertz-comb spectrometer on CMOS for rapid, wide-range gas detection with absolute specificity," *IEEE J. Solid-State Circuits*, vol. 52, no. 12, pp. 3361–3372, Dec. 2017.
- [4] X. Wu and K. Sengupta, "On-chip THz spectroscope exploiting electromagnetic scattering with multi-port antenna," *IEEE J. Solid-State Circuits*, vol. 51, no. 12, pp. 3049–3062, Dec. 2016.
- [5] R. Han and E. Afshari, "A CMOS high-power broadband 260-GHz radiator array for spectroscopy," *IEEE J. Solid-State Circuits*, vol. 48, no. 12, pp. 3090–3104, Dec. 2013.
- [6] R. Han *et al.*, "A SiGe terahertz heterodyne imaging transmitter with 3.3 mW radiated power and fully-integrated phase-locked loop," *IEEE J. Solid-State Circuits*, vol. 50, no. 12, pp. 2935–2947, Dec. 2015.
- [7] P. Hillger, J. Grzyb, R. Jain, and U. R. Pfeiffer, "Terahertz imaging and sensing applications with silicon-based technologies," *IEEE Trans. THz Sci. Technol.*, vol. 9, no. 1, pp. 1–19, Jan. 2019.
- [8] M. Uzunkol, O. D. Gurbuz, F. Golcuk, and G. M. Rebeiz, "A 0.32 THz SiGe 4×4 imaging array using high-efficiency on-chip antennas," *IEEE J. Solid-State Circuits*, vol. 48, no. 9, pp. 2056–2066, Sep. 2013.
- [9] T. Chi, M.-Y. Huang, S. Li, and H. Wang, "17.7 a packaged 90-to-300GHz transmitter and 115-to-325GHz coherent receiver in CMOS for full-band continuous-wave mm-wave hyperspectral imaging," in *IEEE Int. Solid-State Circuits Conf. (ISSCC) Dig. Tech. Papers*, San Francisco, CA, USA, Feb. 2017, pp. 304–305.
- [10] C.-H. Li, C.-L. Ko, M.-C. Kuo, and D.-C. Chang, "A 340-GHz heterodyne receiver front end in 40-nm CMOS for THz biomedical imaging applications," *IEEE Trans. THz Sci. Technol.*, vol. 6, no. 4, pp. 625–636, Jul. 2016.
- [11] A. Mostajeran, A. Cathelin, and E. Afshari, "A 170-GHz fully integrated single-chip FMCW imaging radar with 3-D imaging capability," *IEEE J. Solid-State Circuits*, vol. 52, no. 10, pp. 2721–2734, Oct. 2017.
- [12] A. Visweswaran *et al.*, "9.4 a 145GHz FMCW-radar transceiver in 28nm CMOS," in *IEEE Int. Solid-State Circuits Conf. (ISSCC) Dig. Tech. Papers*, San Francisco, CA, USA, Feb. 2019, pp. 168–169.
- [13] K. Katayama *et al.*, "A 300 GHz CMOS transmitter with 32-QAM 17.5 Gb/s/ch capability over six channels," *IEEE J. Solid-State Circuits*, vol. 51, no. 12, pp. 3037–3048, Dec. 2016.
- [14] S. Kang, S. V. Thyagarajan, and A. M. Niknejad, "A 240 GHz fully integrated wideband QPSK transmitter in 65 nm CMOS," *IEEE J. Solid-State Circuits*, vol. 50, no. 10, pp. 2256–2267, Oct. 2015.
- [15] S. V. Thyagarajan, S. Kang, and A. M. Niknejad, "A 240 GHz fully integrated wideband QPSK receiver in 65 nm CMOS," *IEEE J. Solid-State Circuits*, vol. 50, no. 10, pp. 2268–2280, Oct. 2015.
- [16] S. Lee *et al.*, "9.5 an 80Gb/s 300GHz-band single-chip CMOS transceiver," in *IEEE Int. Solid-State Circuits Conf. (ISSCC) Dig. Tech. Papers*, San Francisco, CA, USA, Feb. 2019, pp. 170–172.
- [17] K. Guo, Y. Zhang, and P. Reynaert, "A 0.53-THz subharmonic injection-locked phased array with $63-\mu$ w radiated power in 40-nm CMOS," *IEEE J. Solid-State Circuits*, vol. 54, no. 2, pp. 380–391, Feb. 2019.
- [18] Y. Yang, O. D. Gurbuz, and G. M. Rebeiz, "An eight-element 370–410-GHz phased-array transmitter in 45-nm CMOS SOI with peak EIRP of 8–8.5 dBm," *IEEE Trans. Microw. Theory Techn.*, vol. 64, no. 12, pp. 4241–4249, Dec. 2016.
- [19] P. Hillger, J. Grzyb, S. Malz, B. Heinemann, and U. Pfeiffer, "A lens-integrated 430 GHz SiGe HBT source with up to 6.3 dBm radiated power," in *Proc. IEEE Radio Freq. Integr. Circuits Symp. (RFIC)*, Honolulu, HI, USA, Jun. 2017, pp. 160–163.

- [20] S. Jameson, E. Halpern, and E. Socher, "20.4 a 300GHz wirelessly locked 2–3 array radiating 5.4dBm with 5.1% DC-to-RF efficiency in 65nm CMOS," in *IEEE Int. Solid-State Circuits Conf. (ISSCC) Dig. Tech. Papers*, San Francisco, CA, USA, Jan. 2016, pp. 348–349.
- [21] Y.-J. Chen and T.-S. Chu, "2-D direct-coupled standing-wave oscillator arrays," *IEEE Trans. Microw. Theory Techn.*, vol. 61, no. 12, pp. 4472–4482, Dec. 2013.
- [22] Y. Tousi and E. Afshari, "A high-power and scalable 2-D phased array for terahertz CMOS integrated systems," *IEEE J. Solid-State Circuits*, vol. 50, no. 2, pp. 597–609, Feb. 2015.
- [23] H. Jalili and O. Momeni, "17.10 a 318-to-370GHz standing-wave 2D phased array in 0.13 μ m BiCMOS," in *IEEE Int. Solid-State Circuits Conf. (ISSCC) Dig. Tech. Papers*, San Francisco, CA, USA, Feb. 2017, pp. 310–311.
- [24] H. Jalili and O. Momeni, "A 0.34-THz wideband wide-angle 2-D steering phased array in 0.13- μ m SiGe BiCMOS," *IEEE J. Solid-State Circuits*, vol. 54, no. 9, pp. 2449–2461, Sep. 2019.
- [25] H. Jalili and O. Momeni, "A standing-wave architecture for scalable and wideband millimeter-wave and terahertz coherent radiator arrays," *IEEE Trans. Microw. Theory Techn.*, vol. 66, no. 3, pp. 1597–1609, Mar. 2018.
- [26] K. Sengupta and A. Hajimiri, "A 0.28 THz power-generation and beam-steering array in CMOS based on distributed active radiators," *IEEE J. Solid-State Circuits*, vol. 47, no. 12, pp. 3013–3031, Dec. 2012.
- [27] Y. Zhao *et al.*, "A 0.54–0.55 THz 2×4 coherent source array with EIRP of 24.4 dBm in 65nm CMOS technology," in *IEEE MTT-S Int. Microw. Symp. Dig.*, Phoenix, AZ, USA, May 2015, pp. 1–3.
- [28] U. R. Pfeiffer *et al.*, "A 0.53 THz reconfigurable source module with up to 1 mW radiated power for diffuse illumination in terahertz imaging applications," *IEEE J. Solid-State Circuits*, vol. 49, no. 12, pp. 2938–2950, Dec. 2014.
- [29] Y. Zhao *et al.*, "A 0.56 THz phase-locked frequency synthesizer in 65 nm CMOS technology," *IEEE J. Solid-State Circuits*, vol. 51, no. 12, pp. 3005–3019, Dec. 2016.
- [30] P. Hillger, J. Grzyb, R. Lachner, and U. Pfeiffer, "An antenna-coupled 0.49 THz SiGe HBT source for active illumination in terahertz imaging applications," in *Proc. 10th Eur. Microw. Integr. Circuits Conf. (EuMIC)*, Paris, France, Sep. 2015, pp. 180–183.
- [31] H. Jalili and O. Momeni, "A 219-to-238-GHz coupled standing-wave VCO with 3.4-dBm peak output power in 65nm CMOS," in *Proc. IEEE Custom Integr. Circuits Conf. (CICC)*, Austin, TX, USA, Apr. 2019, pp. 1–4.
- [32] H. Jalili and O. Momeni, "A 230-GHz high-power and wideband coupled standing wave VCO in 65-nm CMOS," *IEEE J. Solid-State Circuits*, vol. 55, no. 3, pp. 547–556, Mar. 2020.
- [33] D. Pozar, "Considerations for millimeter wave printed antennas," *IEEE Trans. Antennas Propag.*, vol. 31, no. 5, pp. 740–747, Sep. 1983.
- [34] G. M. Rebeiz, "Millimeter-wave and terahertz integrated circuit antennas," *Proc. IEEE*, vol. 80, no. 11, pp. 1748–1770, Nov. 1992.
- [35] A. Safaripour, B. Asghari, M. R. M. Hashemi, and A. Hajimiri, "Proximal-field sensing: *In situ* prediction of far-field radiation for integrated radiators," *IEEE Trans. Microw. Theory Techn.*, vol. 67, no. 9, pp. 3743–3756, Sep. 2019.
- [36] J. M. Edwards and G. M. Rebeiz, "High-efficiency elliptical slot antennas with quartz superstructures for silicon RFICs," *IEEE Trans. Antennas Propag.*, vol. 60, no. 11, pp. 5010–5020, Nov. 2012.
- [37] H.-C. Chang, X. Cao, U. K. Mishra, and R. A. York, "Phase noise in coupled oscillators: Theory and experiment," *IEEE Trans. Microw. Theory Techn.*, vol. 45, no. 5, pp. 604–615, May 1997.
- [38] A. Babakhani, X. Guan, A. Komijani, A. Natarajan, and A. Hajimiri, "A 77-GHz phased-array transceiver with on-chip antennas in silicon: Receiver and antennas," *IEEE J. Solid-State Circuits*, vol. 41, no. 12, pp. 2795–2806, Dec. 2006.
- [39] D. F. Filipovic, S. S. Gearhart, and G. M. Rebeiz, "Double-slot antennas on extended hemispherical and elliptical silicon dielectric lenses," *IEEE Trans. Microw. Theory Techn.*, vol. 41, no. 10, pp. 1738–1749, Oct. 1993.
- [40] D. F. Filipovic, G. P. Gauthier, S. Raman, and G. M. Rebeiz, "Off-axis properties of silicon and quartz dielectric lens antennas," *IEEE Trans. Antennas Propag.*, vol. 45, no. 5, pp. 760–766, May 1997.
- [41] M. Alonso-delPino, C. Jung-Kubiak, T. Reck, N. Llombart, and G. Chattopadhyay, "Beam scanning of silicon lens antennas using integrated piezomotors at submillimeter wavelengths," *IEEE Trans. Terahertz Sci. Technol.*, vol. 9, no. 1, pp. 47–54, Jan. 2019.
- [42] N. Buadana, S. Jameson, and E. Socher, "A 280GHz +9dBm TRP dense 2D multi port radiator in 65nm CMOS," in *Proc. IEEE Radio Freq. Integr. Circuits Symp. (RFIC)*, Philadelphia, PA, USA, Jun. 2018, pp. 248–251.
- [43] Z. Hu, M. Kaynak, and R. Han, "High-power radiation at 1 THz in silicon: A fully scalable array using a multi-functional radiating mesh structure," *IEEE J. Solid-State Circuits*, vol. 53, no. 5, pp. 1313–1327, May 2018.
- [44] K. Guo, A. Standaert, and P. Reynaert, "A 525–556-GHz radiating source with a dielectric lens antenna in 28-nm CMOS," *IEEE Trans. THz Sci. Technol.*, vol. 8, no. 3, pp. 340–349, May 2018.



Hossein Jalili (Member, IEEE) received the B.Sc. and M.S. degrees from the Sharif University of Technology, Tehran, Iran, in 2009 and 2011, respectively, and the Ph.D. degree from the University of California at Davis, Davis, CA, USA, all in electrical engineering in 2019.

He is currently a Post-Doctoral Researcher with the University of California at Davis. His research interests include mm-wave and terahertz integrated circuits and systems in silicon technology.

Dr. Jalili was a recipient of the IEEE Solid-State Circuits Society (SSCS) Predoctoral Achievement Award in 2019, the 2018 IEEE Microwave Theory and Techniques Society (MTT-S) Graduate Fellowship Award, the 2019 University of California at Davis's Allen G. Marr Prize Distinguished Dissertation Award and the 2019 Electrical and Computer Engineering (ECE) Department's Anil Jain Memorial Prize for Best Ph.D. Student Dissertation, the 2018–2019 Richard and Joy Dorf Graduate Student Award, the University of California at Davis Graduate Fellowship Award in 2013, and the 2018–2019 Summer Graduate Student Researcher (GSR) Award. He has served as a Reviewer for multiple technical journals, including the IEEE JOURNAL OF SOLID-STATE CIRCUITS, the IEEE TRANSACTIONS ON MICROWAVE THEORY AND TECHNIQUES, the IEEE TRANSACTIONS ON CIRCUITS AND SYSTEMS—I, and the IEEE TRANSACTIONS ON TERAHERTZ SCIENCE AND TECHNOLOGY.



Omeed Momeni (Senior Member, IEEE) received the B.Sc. degree from the Isfahan University of Technology, Isfahan, Iran, in 2002, the M.S. degree from the University of Southern California, Los Angeles, CA, USA, in 2006, and the Ph.D. degree from Cornell University, Ithaca, NY, USA, in 2011, all in electrical engineering.

He joined the faculty of the Electrical and Computer Engineering Department, University of California at Davis, Davis, CA, USA, in 2011, where he is currently an Associate Professor. He was a Visiting Professor with the Electrical Engineering and Computer Science Department, University of California at Irvine, Irvine, CA, USA, from 2011 to 2012. From 2004 to 2006, he was with the National Aeronautics and Space Administration (NASA), Jet Propulsion Laboratory (JPL), Pasadena, CA, USA, as an RFIC Designer. His research interest includes mm-wave and terahertz integrated circuits and systems.

D. Momeni was an Organizing Committee Member of the IEEE International Workshop on Design Automation for Analog and Mixed-Signal Circuits in 2013. He was a recipient of the National Science Foundation CAREER Award in 2015, the Professor of the Year 2014 by the IEEE at UC Davis, the Best Ph.D. Thesis Award from the Cornell ECE Department in 2011, the Outstanding Graduate Award from the Association of Professors and Scholars of Iranian Heritage (APSIH) in 2011, the Best Student Paper Award at the IEEE Workshop on Microwave Passive Circuits and Filters in 2010, the Cornell University Jacob's Fellowship in 2007, and the NASA-JPL Fellowship in 2003. He has been serving as a Distinguished Lecturer for the Solid-State Circuits Society (SSCS) since 2020, and a Technical Program Committee Member of the International Microwave Symposium (IMS) since 2017 and the Radio Frequency Integrated Circuits (RFIC) Symposium since 2018. He has also served as an Associate Editor for the IEEE TRANSACTIONS ON MICROWAVE THEORY AND TECHNIQUES (TMTT) from 2018 to 2020. He was the Chair of the IEEE Ithaca GOLD Section from 2008 to 2011.